Pressure assisted sintering stress exponent assessment methods: Accuracy analysis and effect of sintering stress

Charles Manière, Joseph Sambasene Diatta, Christelle Harnois, Christophe Couder, Christelle Bilot, Sylvain Marinel

Pressure assisted sintering stress exponent assessment methods: accuracy analysis and effect of sintering stress

Charles Manière[1]*, Joseph Sambasene Diatta[2], Christelle Harnois[1], Christophe Couder[1], Christelle Bilot[1], Sylvain Marinel[1]

1. Normandie Univ, ENSICAEN, UNICAEN, CNRS, CRISMAT, 14000, Caen, France
2. Assane Seck University, Ziguinchor, Sénégal

Keywords
Pressure assisted sintering; Ceramic; Modeling; Creep; Mechanisms

Abstract

Pressure assisted sintering models involve creep based mechanisms having different stress exponent values. The later evolve from linear viscous diffusional creep mechanisms to highly non-linear mechanisms involving dislocation motion. Consequently, the determination of the stress exponent is of key importance to define the sintering mechanisms and one of the first parameters to identify for the assessment of sintering model. Different methods exist in the literature involving tests at different pressures or with a stepwise pressure profile to extract the creep stress sensitivity. Open questions remain on the accuracy of these methods with the impact of sintering stress (high in ceramics nano-powders) or transient microstructure evolution for the stepwise approaches. This accuracy issue is investigated on an alumina submicronic powder by comparing different methods based on sinter-forging and Spark Plasma Sintering (SPS) at 1200°C. We show that the sintering stress has a high influence on the identified value of stress exponent. Otherwise, the combination of sintering stress and transient behavior at the level of the pressure "jump" of the stepwise method can lead to high disturbance in the identified values.

Graphical Abstract

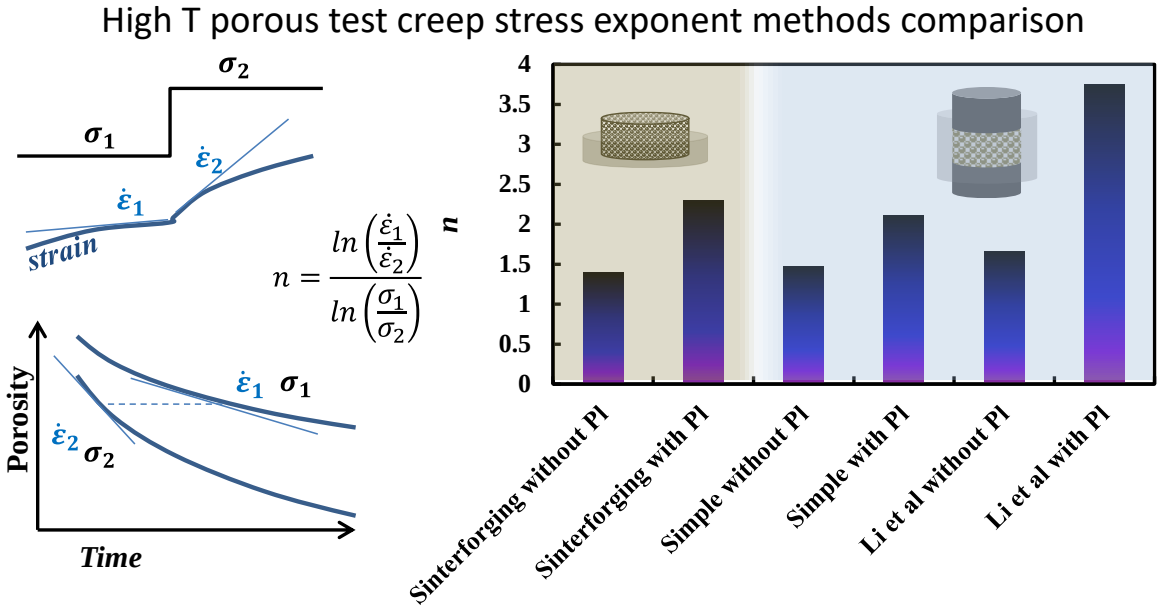

* Corresponding author: **CM**: Laboratoire de cristallographie et sciences des matériaux (CRISMAT), 6 Bvd du maréchal Juin 14050 CAEN CEDEX 4, France
Ph.: +33.2.31.45.13.69 ; *E-mail address*: charles.maniere@ensicaen.fr

Nomenclature

Alphabetical terms and abbreviations

A Creep law deformability term ($Ks^{-1}Pa^{-n}$)
D Diffusion coefficient ($m^2.S^{-1}$)
$\dot{e}$ Trace of the strain rate tensor (s^{-1})
H A constant for creep based hot pressing model
$\mathbb{i}$ Identity tensor
k Boltzmann Constant ($1.380\ 649 \times 10^{-23}$ $J.K^{-1}$)
n Creep law stress exponent
P_l Sintering stress ($N.m^{-2}$)
r, G Particles radius, Grain size (m)
T Temperature (K)
HIP Hot isostatic pressing
SPS Spark Plasma Sintering
HP Hot pressing

Greek symbols

θ Porosity
$\dot{\theta}$ Porosity elimination rate (s^{-1})
ρ Relative density
$\underline{\sigma}$ Stress tensor ($N.m^{-2}$)
σ_{eq} Equivalent stress ($N.m^{-2}$)
$\underline{\dot{\varepsilon}}$ Strain rate tensor (s^{-1})
$\dot{\varepsilon}_{eq}$ Equivalent strain rate (s^{-1})
φ Shear modulus
ψ Bulk modulus
α Surface energy ($J.m^{-2}$)
$\dot{\varepsilon}_z$ Axial strain rate tensor component (s^{-1})
σ_z Axial stress tensor component ($N.m^{-2}$)
θ_c Critical porosity
ϕ Stress intensification factor
$\#_{1\ or\ 2}$ the subscripts 1 or 2 refer to parameters at different pressures

1. Introduction

Pressure assisted sintering includes different methods such as Hot Isostatic Pressing (HIP), Hot Pressing (HP) or faster technique like Spark Plasma Sintering (SPS). These advanced sintering methods allow decreasing the sintering temperature, favor the total elimination of residual porosity and enable the sintering of ultra-refractories having strong covalent bonds that cannot be sintered by pressureless sintering [1–7]. Such conditions allow retaining nano-grain microstructure, producing transparent ceramics or high temperature materials [8–11]. The sintering of these materials involves different sintering mechanisms highly sensitive to the applied stress exponent (called "*n*" in below equation). For instance, the sintering model of HP and SPS is detailed below [6].

$$\frac{1}{\rho}\frac{d\rho}{dt} = -\dot{\varepsilon}_z = \frac{HD(T)\phi(\rho)^n\sigma_z^n}{G^m kT} \quad (1)$$

Where $n = 1$, $m = 2$, corresponds lattice diffusion, $n = 1$, $m = 3$ grain boundary diffusion, $n = 1$ or 2, $m = 1$ grain boundary sliding and $n > 3$, $m = 0$ dislocation creep. The H constant gathers all pre-exponential constants of the underlying creep deformation behavior, the term $\phi(\rho)$ is a relative density function called "stress intensification factor" that describes the porous skeleton effective stress at the grain boundary active zones, and $D(T)$ is the diffusion coefficient which is temperature dependent.

The stress exponent "*n*" governs the degree of non-linearity of the sintering model where linear mechanisms (n=1) are the grain boundary/lattice diffusion and highly nonlinear (n>1) ones are dislocation based mechanisms or grain boundary sliding [1,6,12]. For certain materials like metals, the stress exponent is not constant but may evolve from dislocation mechanisms at low temperature to diffusional mechanisms at higher temperatures [13,14]. Consequently, the experimental determination of the stress exponent is of key importance and is generally the first step of a simulation study. Different methods exist in the literature to identify the stress exponent: (i) the direct regression method, (ii) fully dense creep tests and (iii) porous stage tests.

Direct identification methods are based on logarithmic linear regression of the applied stress [15]. In these approaches, the regression curves assume theoretical functions for the relative density dependence of the stress intensification factor [16]. These methods are direct and require a few tests but the theoretical porosity function may influence the "*n*" determination and imply unstable results [17].

Another method consists of conducting creep tests [18]. The studied powder is first fully sintered into dense specimens that are subjected to creep tests to determine the stress exponent and the temperature behavior [13,19–22]. This method is ideal for large particle metals but for ceramics where the creep behavior is strongly influenced by the grain size [23] ("*m*" exponent in equation (1)), the large sintered grains may imply a very different creep regime.

To solve later issues, different porous stage methods should be preferred to identify the exponent in the low grain growth zone [24]. The identification methods are in isothermal conditions and for temperatures where the grain growth is low ($G^m \sim$ constant) so the terms $\frac{HD(T)}{G^m kT}$ of equation (1) is constant. In addition, the tests compare the sintering shrinkage rate $(\frac{1}{\rho}\frac{d\rho}{dt})$ acceleration at different pressures (σ_z) for similar (or close) relative density (ρ) to negate the influence of the stress intensification factor (ϕ), which is a function of the relative density generally unknown.

Among the existing porous methods which identify the stress exponent by sintering curves, we can cite the "stepwise" approaches and the "constant porosity" multiple tests approach at different pressures. Both approaches principles are represented in figure 1.

The stepwise approach applied different brief pressure "jumps" to identify the "*n*" exponent by the acceleration of the sintering shrinkage strain rate before and after the "jump" [25–28] (see figure 1a). This approach is one of the most simple as it can be performed is one single test. However, the pressure "jump" should be fast to avoid a high relative density variation that would change the value of the stress intensification factor (ϕ) assumed to be constant. Li *et al* [25], present a theoretical approach to take into account the porosity change at the

transient stage of the pressure "jump" by a hypothesis on the sintering moduli. One of the advantages of this method is to allow a fast exploration of the sintering behavior in a wide pressure range. Different use of Li *et al* [25] method can be cited in the literature for the SPS of Mo [29], W [30], different metals, oxides and plastics [26].

The other method compares different isothermal strain rates tests at "constant porosity" and for different pressures (see figure 1b). This method can be applied to SPS, HP [31] and to sinter-forging [24]. Similar to the formula in figure 1b, the "*n*" can be identified by the strain rate/pressure ratio or by a regression approach on three or more tests [32–34]. The "constant porosity" approaches requires more sintering tests but it ensures no disturbance from the stress intensification factor (ϕ) which is relative density dependent. Nevertheless, the sintering time between the tests can be very long and variations of ϕ can still happen at the same porosity if surface diffusion is highly active.

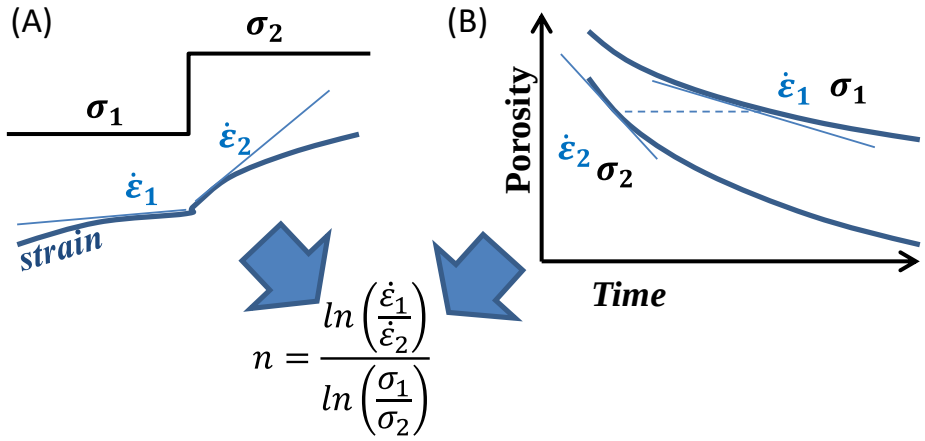

Figure 1 Stress exponent identification methods: stepwise pressure approach (A), multiple pressure isothermal test approach (B)

In summary, the pros and cons of later methods are the following: the "stepwise" is rapid, less influenced by surface diffusion but sensitive to porosity variations, the "constant porosity" method requires multiple tests but assure no disturbance from porosity variation. In this article, the "stepwise" and "constant porosity" methods are tested and compared with SPS and sinter forging methods, respectively. The aim is to verify their accuracy for a submicronic alumina powder sintering. Such a powder has a significant sintering stress (from capillarity

forces) that may have an impact on the identification of the stress exponent. Consequently, the study will also compare the methods with and without the actions of the capillarity forces.

2. Theory and calculations

In this section, "*n*" stress exponent identification analytic equations are detailed for the "stepwise" method applied to SPS and the "constant porosity" method applied to sinter forging. This analysis starts from the general equations of the continuum theory of sintering [35]. In particular the contribution of the sintering stress (P_l) to the "*n*" exponent identification will be detailed for the two methods.

2.1. Stepwise n identification equation for SPS

The general equation describing the continuum theory of sintering behavior is the following:

$$\underline{\sigma} = \frac{\sigma_{eq}}{\dot{\varepsilon}_{eq}}\left(\varphi(\theta)\underline{\dot{\varepsilon}} + \left(\psi(\theta) - \frac{1}{3}\varphi(\theta)\right)\dot{e}\mathbb{i}\right) + P_l\mathbb{i} \quad (2)$$

with Skorohod's theoretical expression of the sintering stress liking the porosity with the surface energy (1.12 J/m^2 for alumina [36]) and the particle radius that can be assumed constant in high porosity tests where grain growth is limited.

$$P_l = \frac{3\alpha}{r}(1-\theta)^2 \quad (3)$$

In SPS case, if the radial displacement is assumed close to zero (die confinement), the specimen temperature is homogeneous and the sintering is in the domain of low grain growth, the above general equation reduces to the following analytical equation [24].

$$\frac{\dot{\theta}}{(1-\theta)} = \dot{\varepsilon}_z = A\left(\psi + \frac{2}{3}\varphi\right)^{\frac{-n-1}{2}}(1-\theta)^{\frac{1-n}{2}}(\sigma_z - P_l)^n \quad (4)$$

Isolating the "*n*" exponent terms we have:

$$\dot{\varepsilon}_z = A\frac{\sqrt{1-\theta}}{\sqrt{\psi+\frac{2}{3}\varphi}}\left(\frac{\sigma_z - P_l}{\sqrt{1-\theta}\sqrt{\psi+\frac{2}{3}\varphi}}\right)^n \quad (5)$$

From later equation, if we assume that the pressure "jump" of the stepwise approach reported in figure 1a implies no porosity variation, the ratio of strain rates before and after the "jump" $\dot{\varepsilon}_1/\dot{\varepsilon}_2$ eliminates all porosity dependent terms (ψ, φ and θ) in equation (5) and the "*n*" exponent can be calculated by the equation below that includes the contribution of P_l.

$$n = \frac{ln\left(\frac{\dot{\varepsilon}_1}{\dot{\varepsilon}_2}\right)}{ln\left(\frac{\sigma_1 - P_l}{\sigma_2 - P_l}\right)} \tag{6}$$

If the transition of pressure implies a porosity evolution which is not negligible ($\theta_2 < \theta_1$), the porosity dependent terms should be considered and the ratio $\dot{\varepsilon}_1/\dot{\varepsilon}_2$ is:

$$\frac{\dot{\varepsilon}_1}{\dot{\varepsilon}_2} = \frac{\sqrt{1-\theta_1}\sqrt{\psi_2+\frac{2}{3}\varphi_2}}{\sqrt{1-\theta_2}\sqrt{\psi_1+\frac{2}{3}\varphi_1}}\left(\frac{(\sigma_1 - P_{l1})\sqrt{1-\theta_2}\sqrt{\psi_2+\frac{2}{3}\varphi_2}}{(\sigma_2 - P_{l2})\sqrt{1-\theta_1}\sqrt{\psi_1+\frac{2}{3}\varphi_1}}\right)^n \tag{7}$$

Isolating the "*n*" term, and taking the logarithm, we have the identification equation below.

$$n = \frac{ln\left(\frac{\dot{\varepsilon}_1}{\dot{\varepsilon}_2}\frac{\sqrt{1-\theta_2}\sqrt{\psi_1+\frac{2}{3}\varphi_1}}{\sqrt{1-\theta_1}\sqrt{\psi_2+\frac{2}{3}\varphi_2}}\right)}{ln\left(\frac{(\sigma_1 - P_{l1})}{(\sigma_2 - P_{l2})}\frac{\sqrt{1-\theta_2}}{\sqrt{1-\theta_1}}\frac{\sqrt{\psi_2+\frac{2}{3}\varphi_2}}{\sqrt{\psi_1+\frac{2}{3}\varphi_1}}\right)} \tag{8}$$

This equation allows considering the small porosity variation during the pressure "jump". This equation is interesting as it allows testing different theoretical hypotheses of shear and bulk moduli. Indeed, the theoretical value of the moduli are often higher than the experimental one that has more energetic and responsive microstructure and then lower values [23,24,37].

If Skorohod [38] theoretical moduli are used, equation (8) becomes the expression below as expressed by Li *et al* [25].

$$n = \frac{ln\left(\sqrt{\frac{(1-\theta_1)\theta_2}{(1-\theta_2)\theta_1}}\frac{|\dot{\varepsilon}_1|}{|\dot{\varepsilon}_2|}\right)}{ln\left(\frac{\sigma_1 - P_{l1}}{\sigma_2 - P_{l2}}\sqrt{\frac{(1-\theta_2)\theta_1}{(1-\theta_1)\theta_2}}\frac{(1-\theta_2)}{(1-\theta_1)}\right)} \tag{9}$$

2.2. Constant porosity n identification method, equations for sinter forging

The analytical formulation of sinter forging is detailed in ref [24]. Assuming homogeneous temperature, a negligible friction with the support and taking into account the sintering stress P_l, the analytic model is the following.

$$\dot{\varepsilon}_z = A\left(\frac{\frac{2|\sigma_z|^2}{3\varphi}+\frac{\left(-\frac{|\sigma_z|}{3}-P_l\right)^2}{\psi}}{1-\theta}\right)^{\frac{n-1}{2}}\left(-\frac{2|\sigma_z|}{3\varphi}+\frac{\left(-\frac{|\sigma_z|}{3}-P_l\right)}{3\psi}\right) \tag{10}$$

The "constant porosity" approach compares two strain rates from two isothermal tests at different pressures and for the same porosity (see figure 1b). Like the "stepwise" approach, below strain rate ratio is used to determine the stress exponent.

$$\frac{\dot{\varepsilon}_1}{\dot{\varepsilon}_2} = \left(\frac{\frac{2|\sigma_1|^2}{3\varphi}+\frac{\left(-\frac{|\sigma_1|}{3}-P_{l1}\right)^2}{\psi}}{\frac{2|\sigma_2|^2}{3\varphi}+\frac{\left(-\frac{|\sigma_2|}{3}-P_{l2}\right)^2}{\psi}}\right)^{\frac{n-1}{2}}\left(\frac{-\frac{2|\sigma_1|}{3\varphi}+\frac{\left(-\frac{|\sigma_1|}{3}-P_{l1}\right)}{3\psi}}{-\frac{2|\sigma_2|}{3\varphi}+\frac{\left(-\frac{|\sigma_2|}{3}-P_{l2}\right)}{3\psi}}\right) \tag{11}$$

Isolating the "*n*" term, we obtain the following identification equation.

$$n = 1+\frac{ln\left(\frac{\dot{\varepsilon}_1}{\dot{\varepsilon}_2}\left(\frac{-\frac{2|\sigma_2|}{3\varphi}+\frac{\left(-\frac{|\sigma_2|}{3}-P_{l2}\right)}{3\psi}}{-\frac{2|\sigma_1|}{3\varphi}+\frac{\left(-\frac{|\sigma_1|}{3}-P_{l1}\right)}{3\psi}}\right)\right)}{ln\sqrt{\frac{\frac{2|\sigma_1|^2}{3\varphi}+\frac{\left(-\frac{|\sigma_1|}{3}-P_{l1}\right)^2}{\psi}}{\frac{2|\sigma_2|^2}{3\varphi}+\frac{\left(-\frac{|\sigma_2|}{3}-P_{l2}\right)^2}{\psi}}}} \tag{12}$$

Because of the presence of the P_l term, the shear and bulk moduli cannot be fully eliminated. Nevertheless, because the analysis compares strain rates at the same porosity, the contributions of the moduli (that are porosity functions) should be negligible and simple Skorohod[38] theoretical functions are used. If the sintering stress P_l is neglected, the moduli terms disappear and the identification expression is as below [24].

$$n = \frac{ln\left(\frac{\dot{\varepsilon}_1}{\dot{\varepsilon}_2}\right)}{ln\left(\frac{\sigma_1}{\sigma_2}\right)} \tag{13}$$

3. Experiment and method

The methodology employed in this paper consists of a comparison of the stress exponent by different methods including stepwise approach conducted on an SPS device and the "constant porosity" approach based on sinter forging tests. A submicronic alumina powder Baikowski® BMA15 with average particle size of 120 nm is used for this study. We use 15 mm diameter punches and 15 mm thick die with heights of 50 mm for the die and 30 mm for the punches. For the stepwise approach, different pressures ranging from 16 MPa to 54 MPa were applied with different 10 MPa pressures "jump" (as short as 10s) at the isothermal temperature of 1200°C. The evolution of the SPS powder height (h) was calculated from the final pellet measured height as reference and the SPS displacement curve (see figure A in appendix). Only the isothermal displacement part was selected to avoid thermal expansion disturbances. From the height curves, the true strain rate curve was determined by $\dot{\varepsilon}_z = \frac{\dot{h}}{h}$. The SPS device "FCT system HPD25" was used with 15 mm inner die and punches. The SPS configuration, calculation of experimental parameters like the strain rate ($\dot{\varepsilon}_z$), the applied stress (σ_z) and the porosity curve (θ) are reported in figure 2a. The profile and the response of the "stepwise" experiment are reported in figure 2b. As shown, the pressure "jump" may implicate a small evolution of the porosity ($\theta_2 < \theta_1$). This evolution can rigidify the porous skeleton and may decrease the value of the measured strain rate after sintering ($\dot{\varepsilon}_2$). To correct this aspect, the shear and bulk moduli generally approximated theoretically (Skorohod [38]) must be actualized ($\varphi_2 > \varphi_1, \psi_2 > \psi_1$ and $P_{l2} > P_{l1}$). The identification equations (6) and (8) reported in figure 2c must be used to identify the "n" in four ways:

(i) The "simple" approach using equation (6) neglecting the porosity evolution and the sintering stress ($P_l = 0$).

(ii) The "simple" approach using equation (6) neglecting the porosity evolution but taking into account P_l.

(iii) The approach using (8) with the porosity variation and neglecting the sintering stress ($P_l = 0$).

(iv) The approach using (8) with the porosity variation and P_l.

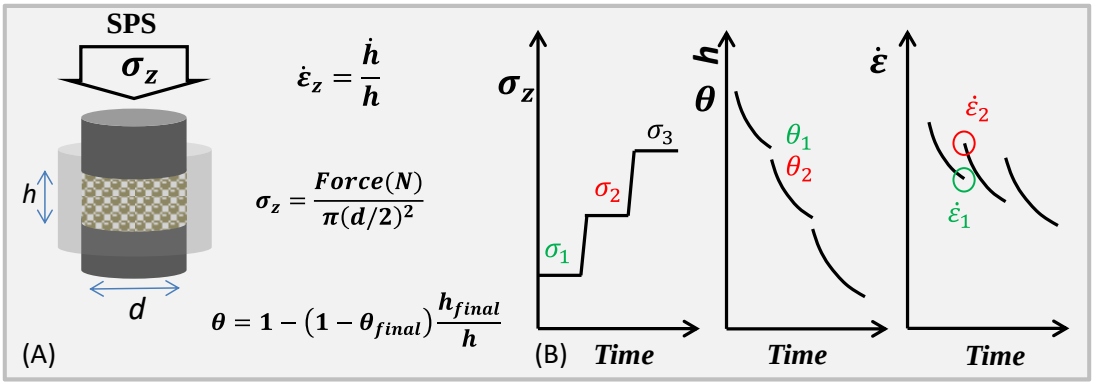

"simple" approach for n identification neglecting the porosity variation at the pressure "jump"

$$n = \frac{ln\left(\frac{\dot{\varepsilon}_1}{\dot{\varepsilon}_2}\right)}{ln\left(\frac{\sigma_1 - P_l}{\sigma_2 - P_l}\right)}$$

(C) **n identification with the porosity variation at the pressure "jump"**

$$n = \frac{ln\left(\frac{\dot{\varepsilon}_1}{\dot{\varepsilon}_2}\frac{\sqrt{1-\theta_2}\sqrt{\psi_1 + \frac{2}{3}\varphi_1}}{\sqrt{1-\theta_1}\sqrt{\psi_2 + \frac{2}{3}\varphi_2}}\right)}{ln\left(\frac{(\sigma_1 - P_{l1})}{(\sigma_2 - P_{l2})}\frac{\sqrt{1-\theta_2}}{\sqrt{1-\theta_1}}\frac{\sqrt{\psi_2 + \frac{2}{3}\varphi_2}}{\sqrt{\psi_1 + \frac{2}{3}\varphi_1}}\right)}$$

Figure 2 Stepwise multiple pressure method applied to SPS, (A) identification of the sintering main variables, (B) typical scheme of the stepwise approach and (C) stress exponent identification equations with and without taking into account the porosity variation during the pressure "jump".

Later four identified *n* values are compared with a method less sensitive to the microstructure evolution, the "constant porosity" method applied to sinter forging. The experiment is implemented in a microwave press device (SAIREM® LABOTRON IWASP2000 2TE) able to apply similar heating profiles as close as possible as SPS ones. The device used is a 2.45 GHz solid-state microwave generator (SAIREM® GMS1000MS) with an auto-adaptive PID regulation (SAIREM® EUROTHERM2408) that controls the temperature of the specimen heated in sinter forging configuration. To ensure a homogeneous heating, SiC microwave susceptors were added to the upper and lower contacts of the specimen and on the two lateral sides (see configuration in figure 3a). A displacement sensor magnescale DS830SLR [39] was used to record the pellet diametric expansion during the test and to

actualize the calculation of the applied stress and the porosity (figure 3a). The principle of the "constant porosity" test is schematically represented in figure 3b. Two tests at 20 and 30 MPa, were performed. Like in the SPS tests, the isothermal temperature was 1200°C. The stress exponent identification uses equations (12) and (13) for identification with and without P_l respectively (see figure 3c).

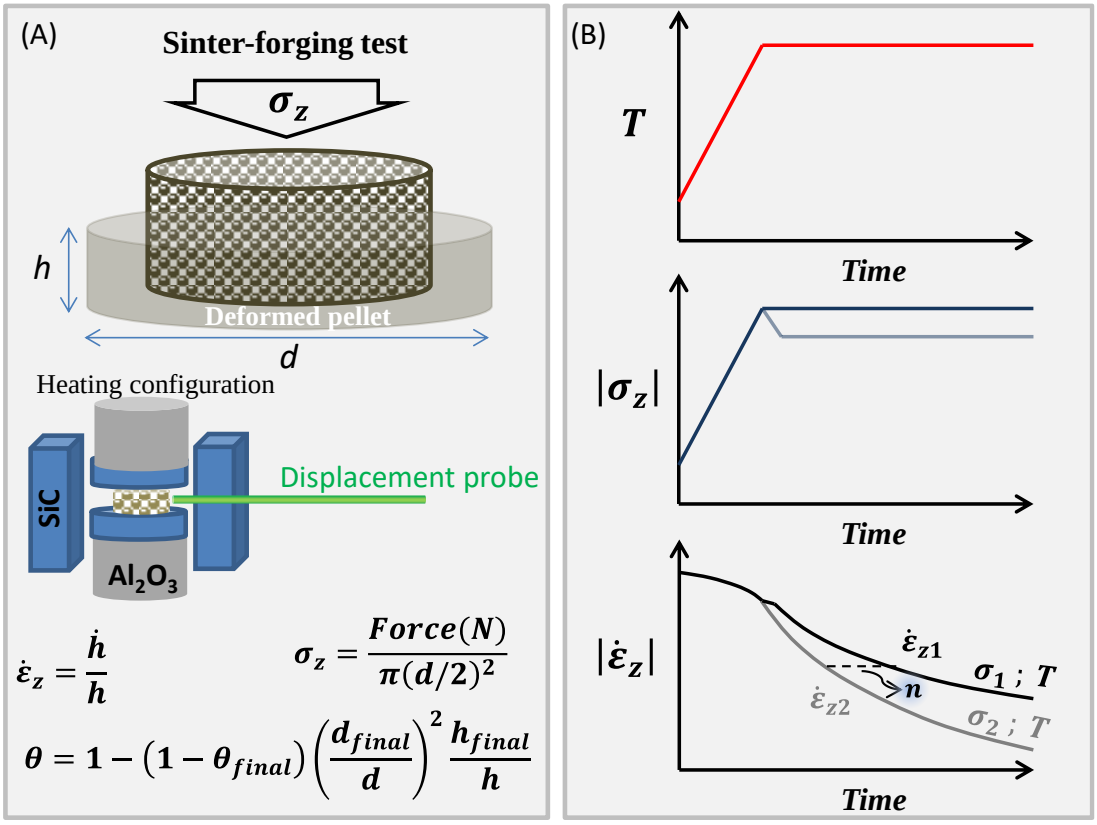

n identification at same porosity neglecting *Pl*

(C)

n identification at same porosity with *Pl*

$$n = \frac{ln\left(\frac{\dot{\varepsilon}_{z1}}{\dot{\varepsilon}_{z2}}\right)}{ln\left(\frac{\sigma_1}{\sigma_2}\right)} \Rightarrow n = 1 + \frac{ln\left(\frac{\dot{\varepsilon}_{z1}}{\dot{\varepsilon}_{z2}}\left(\frac{-\frac{2|\sigma_2|}{3\varphi} + \frac{\left(-\frac{|\sigma_2|}{3} - P_{l2}\right)}{3\psi}}{-\frac{2|\sigma_1|}{3\varphi} + \frac{\left(-\frac{|\sigma_1|}{3} - P_{l1}\right)}{3\psi}}\right)\right)}{ln\sqrt{\frac{\frac{2|\sigma_1|^2}{3\varphi} + \frac{\left(-\frac{|\sigma_1|}{3} - P_{l1}\right)^2}{\psi}}{\frac{2|\sigma_2|^2}{3\varphi} + \frac{\left(-\frac{|\sigma_2|}{3} - P_{l2}\right)^2}{\psi}}}}$$

Figure 3 (A) Scheme of the sinter forging tests with calculation of the main sintering parameter and representation the heating configuration, (B) typical scheme of the constant porosity approach and (C) stress exponent identification equations with and without Pl.

4. Results and discussions

In this section, the results of the two stress exponent identification methods are detailed and compared.

4.1. Sinter-forging based identification of n by the "constant porosity" method

The method presented in figure 3 is applied at 20 and 30MPa for 1200°C. In isobar, isotherm regime, the sinter forging recorded strain rates are reported *vs* porosity in figure 4a. As expected, the strain rate is clearly higher for higher applied stress and in this graph different strain rate ratios have been taken for different fixed porosities. Using the corrected applied stress (which takes into account the specimen diametric expansion), "*n*" stress exponent values have been identified in figure 4b using the equations (12) and (13). The raw experimental data imply a certain noise in the "*n*" values with standard-deviation of 0.8 for the expression with P_l and 0.4 for the one without P_l. The expression (12) with P_l has two main consequences, the noise in the "*n*" data is bigger and the average value of n evolves from 1.4 (for the expression without P_l) to 2.3 for the expression with P_l. From these data, the possible mechanisms are between diffusion (n = 1) and grain boundary sliding (n = 2)[6,12]. For alumina, *n* values close to 1 were identified for field assisted sintering at 1100°C and 1200°C and for 150 nm TMDAR Taimei alumina [32]. For the same powder and at 1000°C, *n* values of 2 and 2.3 where identified for HP and SPS, respectively [33]. These values are identified neglecting the sintering stress P_l. Nevertheless, they are in a similar range to our study. In the following section, the comparison with the stepwise method help discussing the origin of this rise of "*n*" values with P_l (see last section discussion).

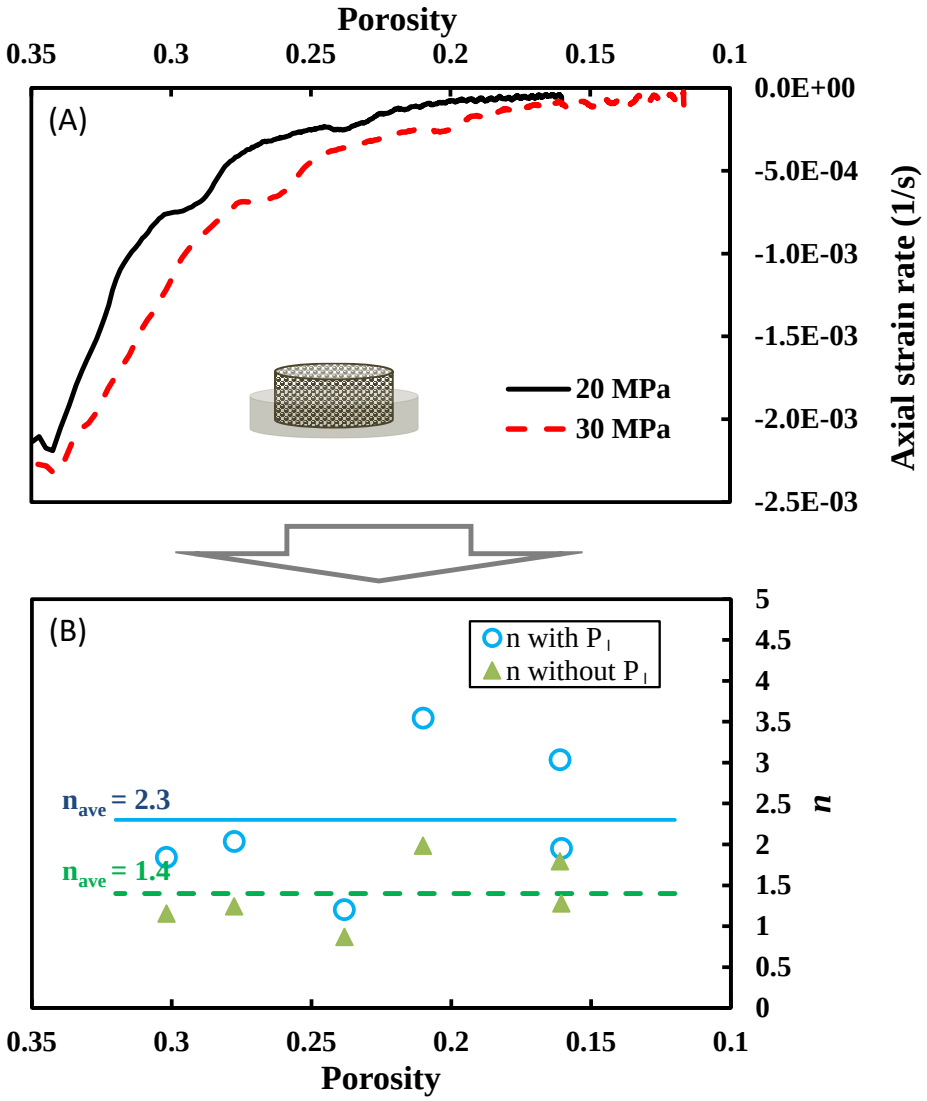

Figure 4 (A) Isobar, isotherm sinter forging strain rate vs specimen porosity, (B) obtained stress exponent with the constant porosity method vs porosity using the equation with and without the P_l term.

4.2. SPS based identification of n by the "stepwise" method

The stepwise method includes one "simple" approach using equation (6) with and without the sintering stress P_l. This equation assumes the pressure "jump" is fast and the porosity evolution before and after the "jump" is nearly the same. However, as Li *et al* [25] showed, the porosity variation can be corrected theoretically using equation (9) based on Skorohod [38] theoretical moduli or equation (8) which allows correcting such moduli function. Indeed, these theoretical moduli like other plasticity/creep based theoretical approaches [40–44] assume spherical porosity which corresponds well to the final stage

sintering but not to the initial stage where the particle contact makes these moduli close to zero. Consequently, in this article we investigate the impact of modified theoretical moduli that correct the initial stage reactivity by a critical porosity inspired from Abouaf *et al* [45,46] moduli function. The modified Skorohod moduli are plotted in figure 5.

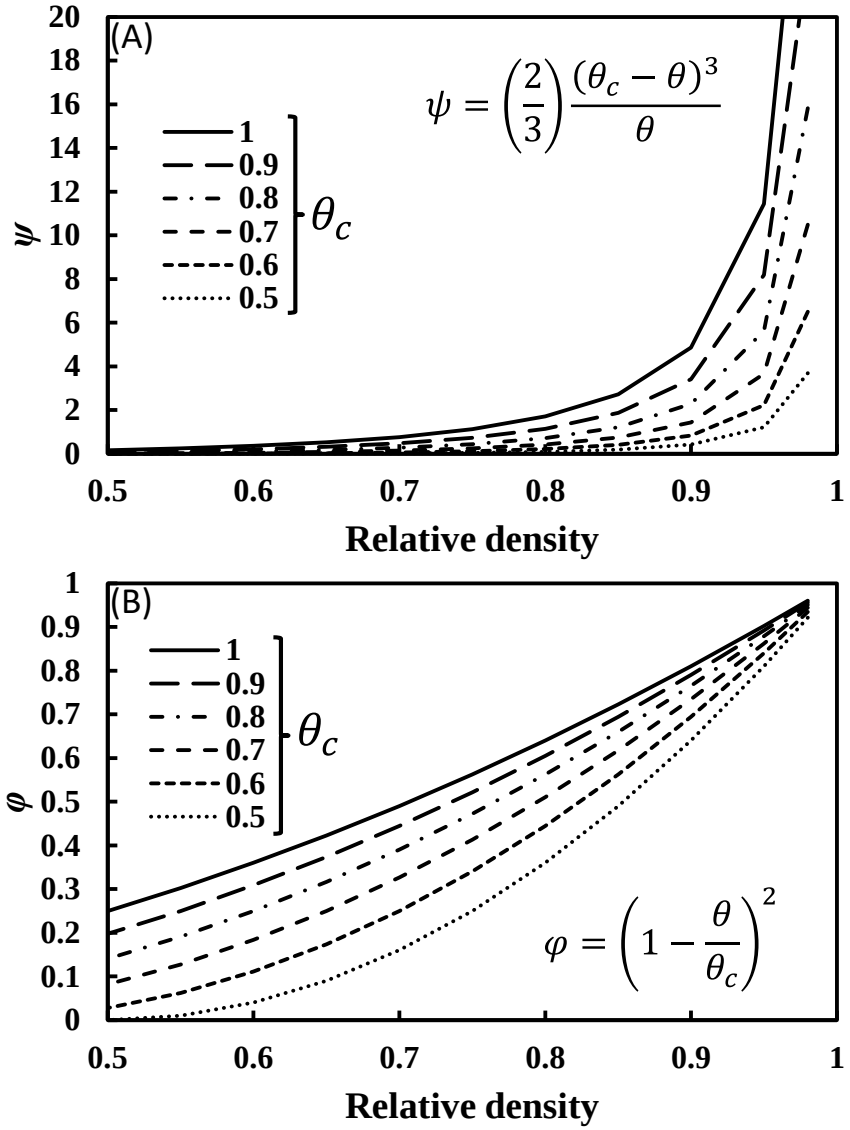

Figure 5 Modified Skorohod moduli for taking into account initial stage sintering high reactivity, (A) bulk modulus, (B) shear modulus.

The recorded SPS specimen height of the 1200°C stepwise experiment is reported in figure 6a. Four successive pressure "jumps" were tested from 16 MPa to 54 MPa. The blue and red parts of the curves indicate the zones of strain rate calculation before and after the pressure "jump". These calculation zones are in isobar/isotherm condition to avoid elastic and

thermal expansion disturbances. The slope of these zones is clearly higher after the rise of pressure. In figure 6b, equation (9) *n* values identified with Skorohod moduli (with and without P_l) are presented. We can clearly see that typical *n* values close the sintering forging tests are found between 0.3 and 0.4 of specimen porosity. However, for porosity lower than 0.3, the moduli make significant disturbances on the *n* values which are out of range. In the same graph, the *n* values identified from the "simple" model of equation (6) that neglects the porosity variation are presented. This model gives much more stable *n* values close to the values between 0.3-0.4 of porosity. The average n values are similar to the sinter forging case with *n* of 2.1 and 1.5 with and without P_l, respectively.

In order to verify if the origin of these disturbances and higher identified *n* values is related to the theoretical moduli that do not correct the initial porosity behavior, the *n* identified with the modified moduli (figure 5) are reported in figure 6c. This clearly shows the correction of the initial stage behavior does not help stable values to be identified. On the contrary, the *n* values become bigger when the critical porosity approaches the initial porosity.

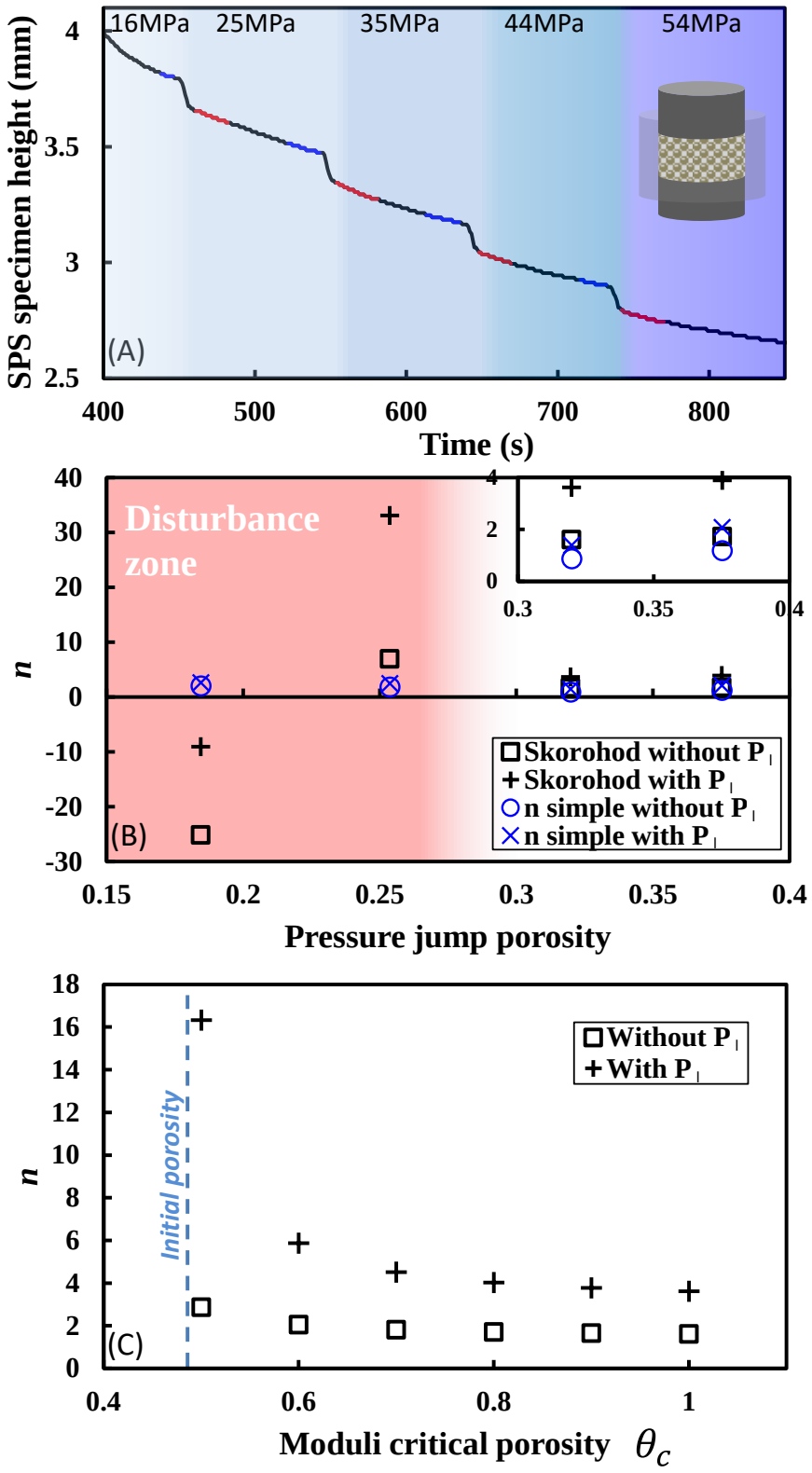

Figure 6 (A) Experimental specimen height evolution for the SPS stepwise experiment at 1200°C, (B) identified n values Skorohod moduli and the simple model that neglects the porosity variation, in the inset, a zoom is made to present the results of "n" values in stability zone, (C) Evolution of n value at 0.32 of porosity for the modified Skorohod moduli with different critical porosity.

4.3. Comparison of the n identified values and discussions

In this section all average *n* values identified by "constant porosity" method (sinter forging) and the "stepwise" method with and without the P_l and the porosity variation are gathered in figure 7. We can see that the value of *n* with and without P_l are very close between the sinter forging and SPS tests. Only the method that considers the porosity variation and P_l shows significantly higher values. For the stepwise approach, considering both P_l sintering stress and the porosity variation seems to make the identification method extremely sensitive to the moduli and unstable in all explored zones. In general, the methods comparison clearly shows the expressions with P_l give higher *n* values. If we consider the fact that the pressure ratio is present at the denominator in equation (6) like in all other identification equations, taking into account the P_l term systematically decreases the denominator and increases the value of *n*. On a mechanistic point of view, high temperatures and low stress favor diffusional mechanisms and *n* close to 1. Conversely, low temperatures and high stresses favor high *n* values of dislocation based mechanisms. The sintering stress (P_l) raises the total effective pressure at the grain boundaries ($\sigma_z - P_l$) as we have $\sigma_z < 0$ for applied compressive stress. Consequently, P_l raises the nonlinear sintering behavior. If the model neglects P_l, it will underestimate both the *n* value and the effective stress. The model predictability of the apparent deformation response will be preserved but it can modify the mechanism interpretation by erroneously indicating diffusional mechanisms with low *n* values close to 1. This is particularly true for submicronic ceramic powders having high sintering stress (P_l~10 MPa). For the special case of the use of nano-size metal powder or composite of nano-size powder the capillarity stress (P_l) should also be considered to avoid underestimate the stress exponent value. Compared to hot pressing, SPS of conductive powders many activate different mechanisms (with different "*n*" and "*A*" parameters) due to the "current effect" on the sintering behavior [28,47,48]. It is also true for the case of high heating rate [49] or flash sintering [50,51].

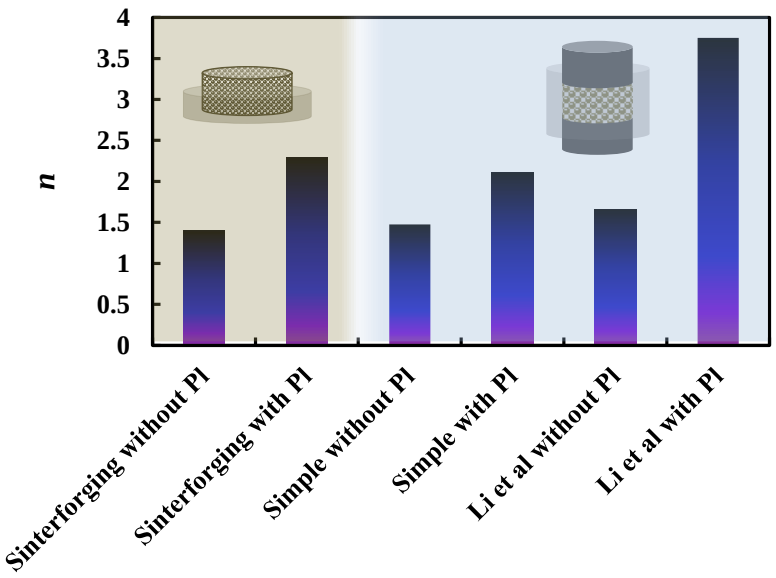

Figure 7 Summary of all average identified n values for all methods.

5. Conclusion

In this study, we present different identification methods of the stress exponent, based on sinter forging and SPS. The methods converge to the same exponent values near 1.4 when neglecting the sintering stress and 2.5 with the sintering stress. For the SPS stepwise approach, taking into account the porosity variation before and after the pressure "jump" seems to destabilize the stress exponent estimation for the low porosity and adding the sintering stress gives even higher out of range exponent values. These instabilities can be explained by an overestimation of the porosity at the pressure "jump". However, considering the identified values of the "simple" model that neglects the porosity evolution gives the same values as sinter-forging method at fixed density, the use of the "simple stepwise" model (which is more stable) is highly recommended. The other main outcome of the study is the impact of the sintering stress that increases the stress exponent in all tested approaches. The sintering stress deserves to be considered in the identification models for nano/submicronic particle size ceramic powder while it can be neglected for large metal particle sintering.

Appendix

In order to determine the strain rate curves of the article, the raw experimental data curves reported in figure A were used.

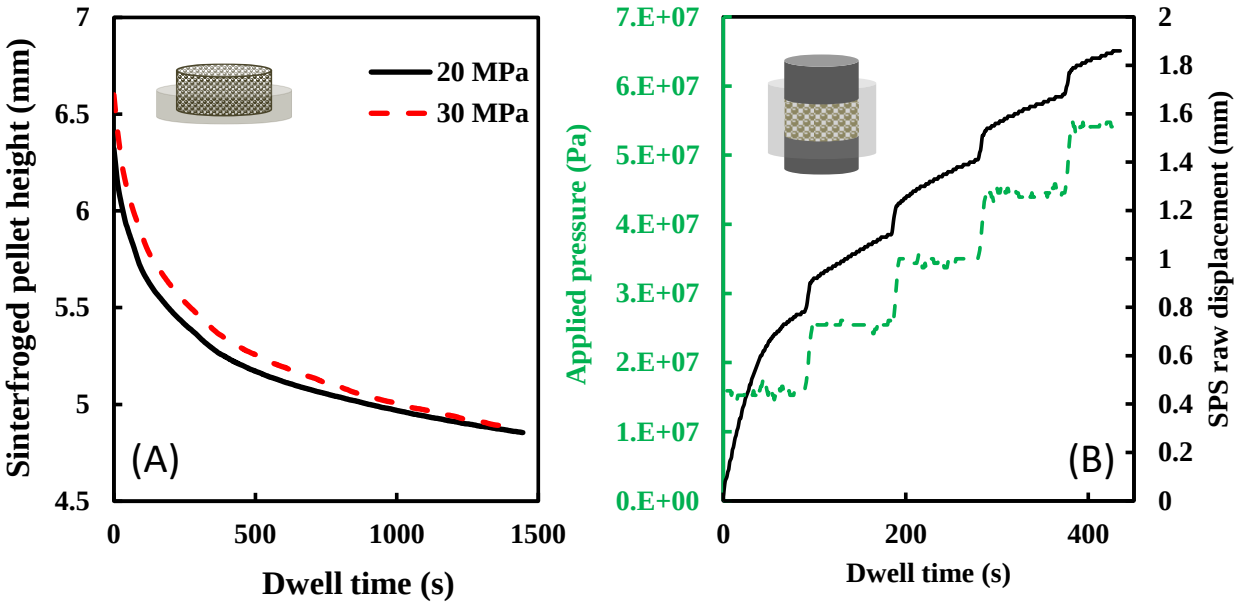

Figure A Main time dependent raw sintering displacement and pressure data for the sinter-forging tests (A) and multiple pressure SPS test (B).

Acknowledgements

The help and support of Jérôme Lecourt and Christelle Bilot is gratefully acknowledged. The project region normandie - 00016601-20E02057_RIN RECHERCHE 2020 - Emergent – ULTIMODULUS support this study.

References

[1] R.K. Bordia, S.-J.L. Kang, E.A. Olevsky, Current understanding and future research directions at the onset of the next century of sintering science and technology, J. Am. Ceram. Soc. 100 (2017) 2314–2352. https://doi.org/10.1111/jace.14919.

[2] S. Grasso, Y. Sakka, G. Maizza, Electric current activated/assisted sintering (ECAS): a review of patents 1906–2008, Sci. Technol. Adv. Mater. 10 (2009) 053001. https://doi.org/10.1088/1468-6996/10/5/053001.

[3] O. Guillon, J. Gonzalez-Julian, B. Dargatz, T. Kessel, G. Schierning, J. Räthel, M. Herrmann, Field-Assisted Sintering Technology/Spark Plasma Sintering: Mechanisms, Materials, and Technology Developments, Adv. Eng. Mater. 16 (2014) 830–849. https://doi.org/10.1002/adem.201300409.

[4] R. Orrù, R. Licheri, A.M. Locci, A. Cincotti, G. Cao, Consolidation/synthesis of materials by electric current activated/assisted sintering, Mater. Sci. Eng. R Reports. 63 (2009) 127–287. https://doi.org/10.1016/j.mser.2008.09.003.

[5] R.M. German, Sintering With External Pressure, in: Sinter. from Empir. Obs. to Sci. Princ., Elsevier, 2014: pp. 305–354. https://doi.org/10.1016/B978-0-12-401682-8.00010-0.

[6] M.N. Rahaman, Sintering of Ceramics, CRC Press, 2007.

[7] B.R. Golla, A. Mukhopadhyay, B. Basu, S.K. Thimmappa, Review on ultra-high temperature boride ceramics, Prog. Mater. Sci. 111 (2020) 100651. https://doi.org/10.1016/j.pmatsci.2020.100651.

[8] Z. Xiao, S. Yu, Y. Li, S. Ruan, L.B. Kong, Q. Huang, Z. Huang, K. Zhou, H. Su, Z. Yao, W. Que, Y. Liu, T. Zhang, J. Wang, P. Liu, D. Shen, M. Allix, J. Zhang, D. Tang, Materials development and potential applications of transparent ceramics: A review, Mater. Sci. Eng. R Reports. 139 (2020) 100518. https://doi.org/10.1016/j.mser.2019.100518.

[9] A. Goldstein, A. Krell, Transparent Ceramics at 50: Progress Made and Further Prospects, J. Am. Ceram. Soc. 99 (2016) 3173–3197. https://doi.org/10.1111/jace.14553.

[10] R. Orrù, G. Cao, Ultra-high temperature ceramics by spark plasma sintering, in: Spark Plasma Sinter., Elsevier, 2019: pp. 49–76. https://doi.org/10.1016/B978-0-12-817744-0.00002-7.

[11] E.A. Olevsky, D. V. Dudina, Field-Assisted Sintering, Springer N, Springer International Publishing, Cham, 2018. https://doi.org/10.1007/978-3-319-76032-2.

[12] R.M. German, Sintering Theory and Practice, Wiley, Wiley, 1996. http://www.wiley.com/WileyCDA/WileyTitle/productCd-047105786X.html.

[13] C. Manière, U. Kus, L. Durand, R. Mainguy, J. Huez, D. Delagnes, C. Estournès, Identification of the Norton-Green Compaction Model for the Prediction of the Ti-6Al-4V Densification During the Spark Plasma Sintering Process, Adv. Eng. Mater. 18 (2016) 1720–1727. https://doi.org/10.1002/adem.201600348.

[14] Y. Xue, L.H. Lang, G.L. Bu, L. Li, Densification modeling of titanium alloy powder during hot isostatic pressing, Sci. Sinter. 43 (2011) 247–260. https://doi.org/10.2298/SOS1103247X.

[15] G. Bernard-Granger, C. Guizard, Spark plasma sintering of a commercially available granulated zirconia powder: I. Sintering path and hypotheses about the mechanism(s) controlling densification, Acta Mater. 55 (2007) 3493–3504. https://doi.org/10.1016/j.actamat.2007.01.048.

[16] A.S. Helle, K.E. Easterling, M.F. Ashby, Hot-isostatic pressing diagrams: New developments, Acta Metall. 33 (1985) 2163–2174. https://doi.org/10.1016/0001-6160(85)90177-4.

[17] P. Guyot, G. Antou, N. Pradeilles, A. Weibel, M. Vandenhende, G. Chevallier, A. Peigney, C. Estournès, A. Maitre, Hot pressing and spark plasma sintering of alumina: Discussion about an analytical modelling used for sintering mechanism determination, Scr. Mater. 84–85 (2014) 35–38. https://doi.org/10.1016/j.scriptamat.2014.04.013.

[18] A.K. Mukherjee, High-Temperature Creep, in: Treatise Mater. Sci. Technol., 1975: pp. 163–224. https://doi.org/10.1016/B978-0-12-341806-7.50010-6.

[19] D. Martins, F. Grumbach, C. Manière, P. Sallot, K. Mocellin, M. Bellet, C. Estournès, In-situ creep law determination for modeling Spark Plasma Sintering of TiAl 48-2-2 powder, Intermetallics. 86 (2017) 147–155. https://doi.org/10.1016/j.intermet.2017.03.006.

[20] C. Nicolle, PhD, Mise en forme de poudre de bore par compression isostatique à chaud: determination des propriétés rhéologiques et simulation numérique du procédé, Université de Bourgogne, France, 1999.

[21] C. Geindreau, D. Bouvard, P. Doremus, Constitutive behaviour of metal powder during hot forming. Part I: Experimental investigation with lead powder as a simulation material, Eur. J. Mech. - A/Solids. 18 (1999) 581–596. https://doi.org/10.1016/S0997-7538(99)00102-3.

[22] M. Abouaf, J.L. Chenot, A numerical model for hot deformation of metal powders, J. Theor. Appl. Mech. 5 (1986) 121–140.

[23] J. Besson, M. Abouaf, Rheology of Porous Alumina and Simulation of Hot Isostatic Pressing, J. Am. Ceram. Soc. 75 (1992) 2165–2172. https://doi.org/10.1111/j.1151-2916.1992.tb04479.x.

[24] C. Manière, C. Harnois, S. Marinel, Porous stage assessment of pressure assisted

sintering modeling parameters: a ceramic identification method insensitive to final stage grain growth disturbance, Acta Mater. 211 (2021) 116899. https://doi.org/10.1016/j.actamat.2021.116899.

[25] W. Li, E.A. Olevsky, J. McKittrick, A.L. Maximenko, R.M. German, Densification mechanisms of spark plasma sintering: multi-step pressure dilatometry, J. Mater. Sci. 47 (2012) 7036–7046. https://doi.org/10.1007/s10853-012-6515-y.

[26] C. Manière, L. Durand, G. Chevallier, C. Estournès, A spark plasma sintering densification modeling approach: from polymer, metals to ceramics, J. Mater. Sci. 53 (2018) 7869–7876. https://doi.org/10.1007/s10853-018-2096-8.

[27] G. Lee, C. Manière, J. McKittrick, A. Gattuso, C. Back, E.A. Olevsky, Oxidation effects on spark plasma sintering of molybdenum nanopowders, J. Am. Ceram. Soc. 102 (2019) 801–812. https://doi.org/10.1111/jace.16182.

[28] G. Lee, E.A. Olevsky, C. Manière, A. Maximenko, O. Izhvanov, C. Back, J. McKittrick, Effect of electric current on densification behavior of conductive ceramic powders consolidated by spark plasma sintering, Acta Mater. 144 (2018) 524–533. https://doi.org/10.1016/j.actamat.2017.11.010.

[29] G. Lee, C. Manière, J. McKittrick, R. Doerner, D. Nishijima, A. Gattuso, T. Abrams, D. Thomas, C. Back, E.A. Olevsky, Consolidation of Molybdenum nanopowders by spark plasma sintering: Densification mechanism and first mirror application, J. Nucl. Mater. 516 (2019). https://doi.org/10.1016/j.jnucmat.2019.01.028.

[30] G. Lee, J. McKittrick, E. Ivanov, E.A. Olevsky, Densification mechanism and mechanical properties of tungsten powder consolidated by spark plasma sintering, Int. J. Refract. Met. Hard Mater. 61 (2016) 22–29. https://doi.org/10.1016/j.ijrmhm.2016.07.023.

[31] G. Lee, C. Manière, J. McKittrick, E.A. Olevsky, Electric current effects in spark plasma sintering: From the evidence of physical phenomenon to constitutive equation formulation, Scr. Mater. 170 (2019) 90–94. https://doi.org/10.1016/j.scriptamat.2019.05.040.

[32] J. Langer, M.J. Hoffmann, O. Guillon, Direct comparison between hot pressing and electric field-assisted sintering of submicron alumina, Acta Mater. 57 (2009) 5454–5465. https://doi.org/10.1016/j.actamat.2009.07.043.

[33] G. Antou, P. Guyot, N. Pradeilles, M. Vandenhende, A. Maître, Identification of densification mechanisms of pressure-assisted sintering: application to hot pressing and

spark plasma sintering of alumina, J. Mater. Sci. 50 (2015) 2327–2336. https://doi.org/10.1007/s10853-014-8804-0.

[34] W.G. Fahrenholtz, G.E. Hilmas, R. Li, Densification of ultra-refractory transition metal diboride ceramics, Sci. Sinter. 52 (2020) 1–14. https://doi.org/10.2298/SOS2001001F.

[35] E.A. Olevsky, Theory of sintering: from discrete to continuum, Mater. Sci. Eng. R Reports. 23 (1998) 41–100. https://doi.org/10.1016/S0927-796X(98)00009-6.

[36] E.A. Olevsky, C. Garcia-Cardona, W.L. Bradbury, C.D. Haines, D.G. Martin, D. Kapoor, Fundamental Aspects of Spark Plasma Sintering: II. Finite Element Analysis of Scalability, J. Am. Ceram. Soc. 95 (2012) 2414–2422. https://doi.org/10.1111/j.1551-2916.2012.05096.x.

[37] C. Wolff, S. Mercier, H. Couque, A. Molinari, Modeling of conventional hot compaction and Spark Plasma Sintering based on modified micromechanical models of porous materials, Mech. Mater. 49 (2012) 72–91. https://doi.org/10.1016/j.mechmat.2011.12.002.

[38] V.V. Skorohod, Rheological basis of the theory of sintering, Nauk. Dumka, Kiev. (1972).

[39] C. Manière, C. Harnois, G. Riquet, T. Grippi, S. Behar-Lafenetre, S. Marinel, Rapid microwave sintering of centimetric zirconia: Scalability and electromagnetic-thermal-fluid-dynamic simulation, J. Am. Ceram. Soc. (2022). https://doi.org/10.1111/jace.18787.

[40] R.J. Green, A plasticity theory for porous solids, Int. J. Mech. Sci. 14 (1972) 215–224. https://doi.org/10.1016/0020-7403(72)90063-X.

[41] P. Sofronis, R.M. McMeeking, Creep of Power-Law Material Containing Spherical Voids, J. Appl. Mech. 59 (1992) S88. https://doi.org/10.1115/1.2899512.

[42] P.P. Castañeda, The effective mechanical properties of nonlinear isotropic composites, J. Mech. Phys. Solids. 39 (1991) 45–71. https://doi.org/10.1016/0022-5096(91)90030-R.

[43] Z.-Z. Du, A.C.F. Cocks, Constitutive models for the sintering of ceramic components—I. Material models, Acta Metall. Mater. 40 (1992) 1969–1979. https://doi.org/10.1016/0956-7151(92)90183-F.

[44] A.C.F. Cocks, Inelastic deformation of porous materials, J. Mech. Phys. Solids. 37 (1989) 693–715. https://doi.org/10.1016/0022-5096(89)90014-8.

[45] M. Abouaf, PhD, Modélisation de la compaction de poudres métalliques frittées, approches par la mécanique des milieux continus, Institut national polytechnique de Grenoble, 1985.

[46] M. Abouaf, J.L. Chenot, G. Raisson, P. Bauduin, Finite element simulation of hot isostatic pressing of metal powders, Int. J. Numer. Methods Eng. 25 (1988) 191–212. https://doi.org/10.1002/nme.1620250116.

[47] G. Lee, C. Manière, J. McKittrick, E.A. Olevsky, Electric current effects in spark plasma sintering: From the evidence of physical phenomenon to constitutive equation formulation, Scr. Mater. 170 (2019). https://doi.org/10.1016/j.scriptamat.2019.05.040.

[48] E. Olevsky, L. Froyen, Constitutive modeling of spark-plasma sintering of conductive materials, Scr. Mater. 55 (2006) 1175–1178. https://doi.org/10.1016/j.scriptamat.2006.07.009.

[49] E.A. Olevsky, S. Kandukuri, L. Froyen, Consolidation enhancement in spark-plasma sintering: Impact of high heating rates, J. Appl. Phys. 102 (2007) 114913. https://doi.org/10.1063/1.2822189.

[50] C. Manière, G. Lee, E.A. Olevsky, All-Materials-Inclusive Flash Spark Plasma Sintering, Sci. Rep. 7 (2017) 15071. https://doi.org/10.1038/s41598-017-15365-x.

[51] C. Manière, C. Harnois, S. Marinel, Role of microstructure reactivity and surface diffusion in explaining flash (ultra-rapid) sintering kinetics, J. Eur. Ceram. Soc. 43 (2023) 2057–2068. https://doi.org/10.1016/j.jeurceramsoc.2022.12.006.